IAC-21-A6.3.7

# Investigation of ENVISAT catastrophic fragmentation scenarios

**Lorenzo Olivieri[a]*, Cinzia Giacomuzzo[b], Cristina Duran[c], Lorenzo Giudici[d], Camilla Colombo[e], Alessandro Francesconi[f]**

[a] *CISAS "G. Colombo", University of Padova, Via Venezia 15, 35131 Padova (PD), Italy,* lorenzo.olivieri@unipd.it
[b] *DII, University of Padova, Via Venezia 1, 35131 Padova (PD), Italy,* cinzia.giacomuzzo@unipd.it
[c] *Politecnico di Milano, Milano, Italy, Email:* cristina.duran@mail.polimi.it
[d] *Politecnico di Milano, Milano, Italy, Email:* lorenzo1.giudici@polimi.it
[e] *Politecnico di Milano, Milano, Italy, Email:* camilla.colombo@polimi.it
[f] *DII/CISAS, University of Padova, Via Venezia 1, 35131 Padova (PD), Italy,* alessandro.francesconi@unipd.it
* Corresponding Author

**Abstract**

ENVISAT is currently one of the largest debris in Low Earth Orbit and it resides in a highly populated orbital zone with higher impact risk. A collision with other satellites or rocket stages could generate and scatter fragments into altitudes occupied by many operational spacecraft, and in the worst case could restrict the access to polar orbits at about 800 km of altitudes. In this context, there is a need to evaluate the contamination of the orbital regions possibly involved by the spread of debris originated after a possible ENVISAT fragmentation. To this aim, this paper presents the results of a campaign of hypervelocity impact simulations with ENVISAT as target, performed with a tool called CSTS (Collision Simulation Tool Solver). The key features of CSTS are the capability of modelling a large variety of collision scenarios involving complex systems such as entire satellites and the possibility to provide statistically accurate results with a computational effort lower than hydrocodes. The simulated collision configurations include two different impacting bodies (small-class 100 kg satellite, defunct rocket stage), two impact positions (glancing impact on ENVISAT radiator, collision on the central body), and two impact velocities (1 and 10 km/s). For each impact configuration, fragments area to mass, characteristic lengths, and velocity distributions are reported and the severity of different collision scenarios is discussed. Based on the said distributions, a second part of the paper focuses on debris cloud evolution and its propagation to other orbits in terms of local variation of the space debris density. This is achieved by superimposing the ENVISAT fragments to the ESA MASTER population and computing the evolution though the Starling suite. For each simulated configuration, local distribution peaks are pointed out and the general deterioration trend of the space debris environment is discussed.

**Keywords:** Space debris, EMR, Catastrophic fragmentation, Space debris environment

## 1. Introduction

The risk of space debris was firstly recognised in the 1970s [1] and the sustainability of the near-Earth orbits [2][3][4] is currently scrutinized due to the continuous small satellites market growth [5][6] and the commercial plans for large constellations deployment [7][8][9][10]. In particular, the probability of massive collisions among satellites is directly related to the number of spacecraft in orbit [11]; this can act as starting point for cascade events affecting the whole near-Earth environment. In fact, past episodes such as the Cosmos-Iridium one [12] showed that the generated fragments are not limited to the involved altitudes but can contaminate neighbourhood orbits.

Lists of potential worst offenders, i.e. resident objects whose fragmentation might cause catastrophic contamination of near-Earth orbits, have been investigated by the scientific community [13][14][15]; these studies indicate the relict of ENVISAT among the most dangerous ones. This Earth observation spacecraft (Fig. 1) operated at an altitude of 800 km; it weighed about 7 ton and consisted of a main body (about 10x5x5 $m^3$) with a large solar panel (14x5 $m^2$) as appendage [16][17]. Communications with ENVISAT were lost in 2012, probably due to a small debris impact; to date the satellite is uncontrolled and it is slowly tumbling [18][19]. Its expected natural decay time is more than 150 years. In addition, ENVISAT orbit is already crowded with both controlled and uncontrolled objects: before the unexpected mission termination, the spacecraft performed a few collisions avoidance manoeuvres [20], that the defunct satellite cannot execute anymore. For these reasons, ENVISAT ranks among the first positions for future Active Debris Removal missions [21][22][23].

Consequently, there is a need to evaluate the contamination of the orbital regions affected by the spread of debris originated after a possible ENVISAT

Fig. 1: ENVISAT artistic representation [17]

fragmentation. To date, with the exception of preliminary results related to this work [24], no detailed model of the spacecraft fragmentation is available in literature, as any fragments distribution is strongly influenced by the collision scenario. Without these models, the propagation of the fragments population generated by a potential collision with ENVISAT cannot be performed. In this context, this paper aims to investigate different collision scenarios, varying the impacting body as well as the impact position, and to propagate the newly generated fragments to identify and assess local variations of the space debris density.

The investigation of the collision events is performed with a proprietary software called Collision Simulation Tool Solver (CSTS) [25]. The key features of CSTS are the capability of modelling a large variety of collision scenarios involving complex systems such as entire satellites and the possibility to provide statistically accurate results with a computational effort orders of magnitude lower than hydrocodes. The CSTS was successfully subjected to a first validation campaign involving both simple targets (plates, Whipple Shields) and sub-scale satellite models [25], demonstrating the capability of well reproducing the experiments outcomes. In addition, the tool was employed in parametric studies to evaluate the transition from low to hypervelocity impacts [26] and the effect of structural integrity on fragmentation processes [27].

The generated debris distributions are used as input to describe the evolution of the fragmentation clouds in the orbital environment. A continuum methodology proposed in [28], is here employed to investigate the time evolution of the debris band.

### *1.1 Paper contents*

This paper is organised as follows. The spacecraft models implemented in the CSTS and the investigated collision scenarios are described in Section 2. Section 3 introduces simulations results and compares the generated fragments distributions with the NASA SBM. The fragmentation cloud propagation model is introduced in Section 4 and the application to the investigated collision scenarios is presented in Section 5.

## 2 Spacecraft models and collision scenarios

The collision scenarios selected for this paper intend to explore the effect of impact velocity, impact point, and impacting body on ENVISAT fragmentation. It is currently assumed that catastrophic impacts (i.e. causing the total fragmentation of the impacted body) occur when the kinetic energy of the impactor is higher than 40 Joule per unit mass of the target (energy-to-mass ratio EMR>40 J/g). The selected configurations include impacts whose EMRs are both below and over this threshold. In addition, models such as the NASA SBM do not contemplate potential dissipation effects in glancing impacts; considering that the Iridium-Cosmos event has been speculated to be a glancing impact, it is worth to investigate collisions both on ENVISAT centre of mass and appendages. Two different impactors are selected, a small-class 100 kg satellite based on JAXA SDS-1 [29], and a rocket stage based on the 4-ton second stage of the Long March CZ2C [30].

### *2.1 ENVISAT model*

A custom-made geometric model of ENVISAT is employed as target in the CSTS simulations. The model features the same elements of the real spacecraft, with structural components, the solar array, and the scientific instrumentation [16][17]. The spacecraft geometric model in CST is shown in Fig. 2. It contains 223 Macroscopic Elements, reproducing the subsystems and the systems specified in Table 1 [17]. The baseline choice for elements' material is

Table 1: ENVISAT geometric model characteristics and elements (data from [17])

| | | |
|---|---|---|
| **Mass** | > 8000 kg | |
| **Main body size** | 1.6 x 2.8 x 1.6 m | |
| **Service module size** | 2.4 x 2.8 x 2.1 m | |
| **Solar array size** | 1.0 x 5.0 x 0.00175 m | |
| **Main components** | XBAND ANTENNA | |
| | STAR TRACKER | |
| | PAYLOAD MODULE CENTRAL TUBE | |
| | TANKS | |
| | BATTERIES | |
| | ELETTRONICS | |
| **Instrumentation** | ASAR | DORIS |
| | RA | MERIS |
| | DRS | MIPAS |
| | MWR | AATSR |
| | GOMOS | SCIAMACHY |

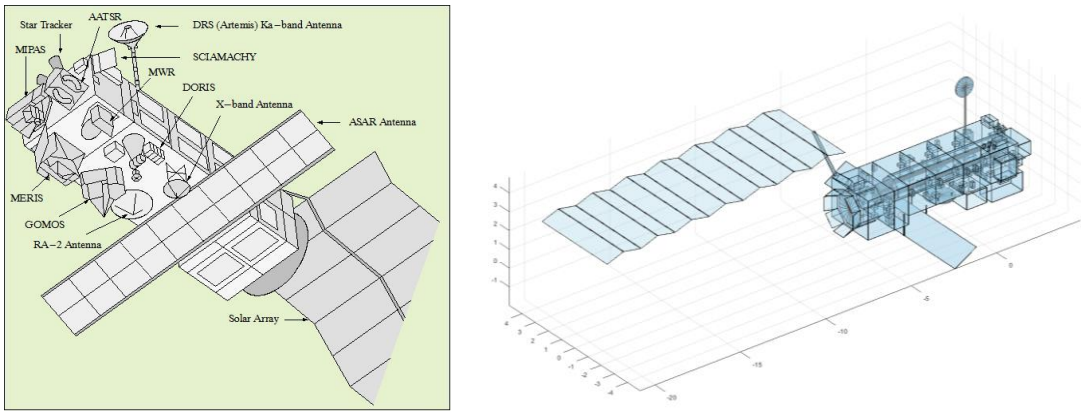


Fig. 2: ENVISAT main elements (left) [17] and CSTS model (right)

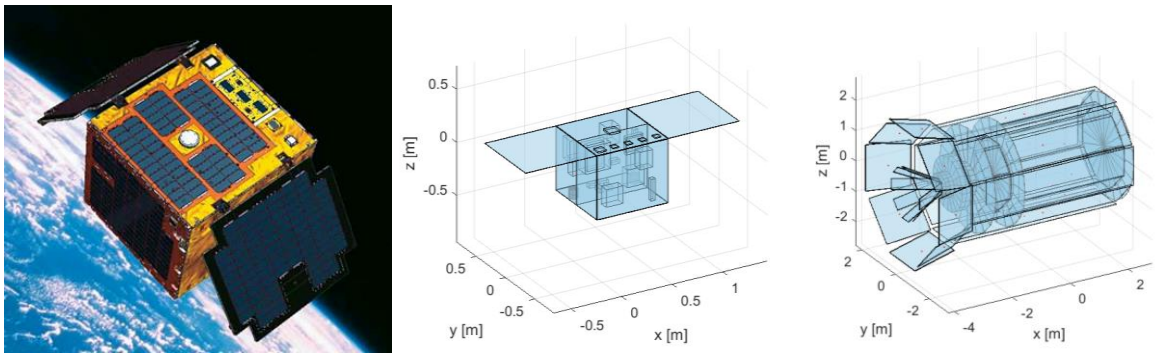


Fig. 3: JAXA SDS-1 artistic representation (left, [29]) and CSTS geometric model (centre); Long March CZ2C second stage CSTS geometric model (right).

aluminium alloy, since it features a ductile structural behaviour, while solar panels are CFRP to simulate a brittle fracture. In some cases, where subsystems incorporating multiple materials and/or multiple components are concerned (propellant tanks, batteries, electronic boxes), the density is reduced to the elements "equivalent density" that matches the real mass of the component. The links connecting Macroscopic Elements are modelled to represent the mechanical connections between the real S/C components.

### *2.2 Impactors models*

The small satellite is based on the 100 kg JAXA SDS-1 spacecraft [29] and can be seen in Fig. 3, left. Its size is 70cm×70cm×60cm. Design details are available online for this spacecraft, that was already modelled for validation simulations in CSTS. The geometric model can be seen in Fig. 3 (centre) and consists of 35 linked macroscopic elements; the selected materials are again aluminium and CFRP.

The rocket stage model (Fig. 3, right) is based on the 4-ton second stage of the Long March CZ2C. The geometric model consists in 49 aluminium linked Macroscopic Elements. Complex features such as the nozzle are simplified with a series of radial plates. In some cases, where subsystems incorporating multiple materials and/or multiple components are concerned, an equivalent thickness is considered for the elements to match the real mass of the component.

### *2.3 Collision scenarios*

Eight collision scenarios are examined; in addition to the two different impactors (small satellite and rocket stage) and the two impact points (ENVISAT centre of mass and appendage), two impact velocities are considered (1 and 10 km/s). Table 2 shows the eight simulated configurations, reporting for each case the impact EMR; it shall be noted that the EMR calculation is not affected by the impact point. The 1 km/s collisions envisage an EMR below the 40 kJ/kg classic catastrophic threshold; in particular, the configuration with the small satellite as impactor is well below such threshold, while the rocket stage scenario provides an intermediate situation with an EMR of about 31 kJ/kg. close to the threshold. For the second velocity, the EMR is always over the catastrophic threshold.

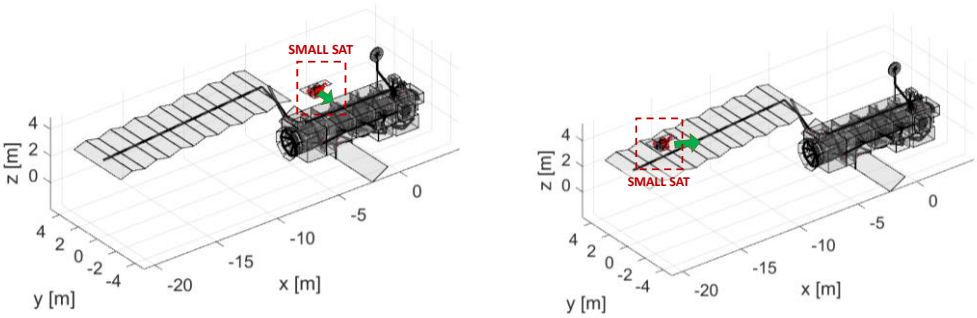


Fig. 4: Small sat impacts on ENVISAT centre of mass (configurations E1 and E3, left) and appendage (configurations E2 and E4, right)

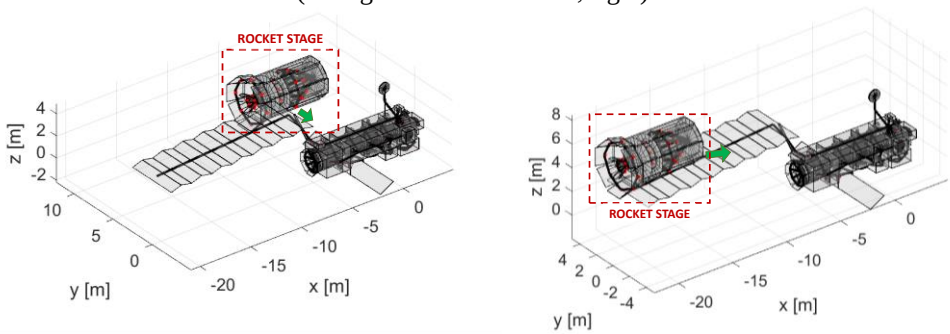


Fig. 5: Rocket stage impacts on ENVISAT centre of mass (configurations E5 and E7, left) and appendage (configurations E6 and E8, right).

The simulated scenarios are shown in Fig. 4 and Fig. 5. According to the NASA SBM, the two impact points (ENVISAT centre of mass and appendage) lead to the same result in terms of objects' fragmentation for a given EMR, since the total mass of the event is the same in both situations. However, the involvement of appendages may contribute to dampen the impact energy, and hence different impact consequences are expected in the two cases.

Table 2: List of the simulated impact scenarios

| Sim. ID | Impactor | Impact velocity, km/s | Impact point | EMR, kJ/kg |
|---|---|---|---|---|
| E-1 | Small Sat | 1 | Central body | 0.78 |
| E-2 | Small Sat | 1 | Appendage | |
| E-3 | Small Sat | 10 | Central body | 78.1 |
| E-4 | Small Sat | 10 | Appendage | |
| E-5 | Rocket stage | 1 | Central body | 31.3 |
| E-6 | Rocket stage | 1 | Appendage | |
| E-7 | Rocket stage | 10 | Central body | 3125.0 |
| E-8 | Rocket stage | 10 | Appendage | |

## 3 Collision simulations results

In this section the main results collected from the eight simulations are reported. For each simulation, a minimum resolution of 1 cm was imposed for debris size (i.e. debris with all dimensions <1 cm were not considered individually but as a debris cloud and are not included in the following results).

Table 3 reports the number of fragments at the end of simulations; it can be noted that fragments order of magnitude is related to the EMR, with low-energy impacts (E-1 and E-2) generating about 2000 fragment, and high-energy collision scenarios (E-7 and E-8) producing more than 90000 secondary debris. In addition, it can be noted that impacts on the central body usually generate less fragments than collisions on ENVISAT appendage; only the lowest energy impacts (E-1 and E-2) show a comparable number of fragments, with a slight lead for case E-1.

Table 3: Number of fragments >1 cm

| Simulation ID | EMR, kJ/kg | Number of fragments > 1 cm | | |
|---|---|---|---|---|
| | | ENVISAT | Impactor | Total |
| E-1 | 0.78 | 877 | 1328 | 2205 |
| E-2 | | 1577 | 329 | 1906 |
| E-3 | 78.1 | 5816 | 6107 | 11923 |
| E-4 | | 14757 | 3843 | 18600 |
| E-5 | 31.3 | 2231 | 1470 | 3700 |
| E-6 | | 11723 | 3715 | 15437 |
| E-7 | 3125.0 | 67404 | 23323 | 90726 |
| E-8 | | 98476 | 24480 | 123356 |

### *3.1 Characteristic length distributions*

Fig. 6 and Fig. 7 report the characteristic length cumulative distributions for the eight collision

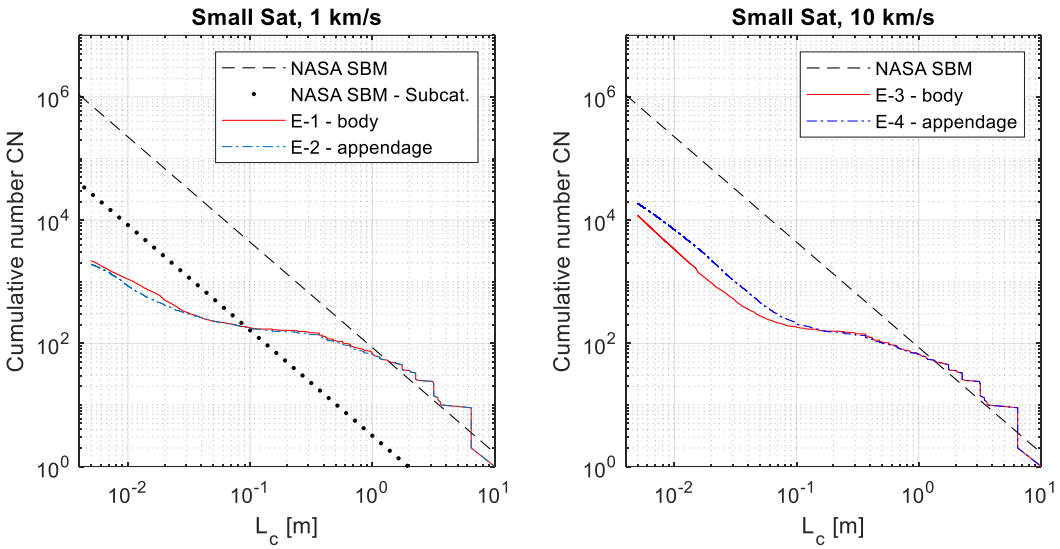


Fig. 6: $L_C$ distribution curves for the small satellite impact on ENVISAS at 1 km/s (left, compared to NASA SBM, dashed black line, and NASA SBM subcatastrophic, dotted black line) and at 10 km/s (right, compared to NASA SBM, dashed black line). Impact on ENVISAT centre of mass is reported with the red solid line, impact on the appendage with the blue dashed-dotted line.

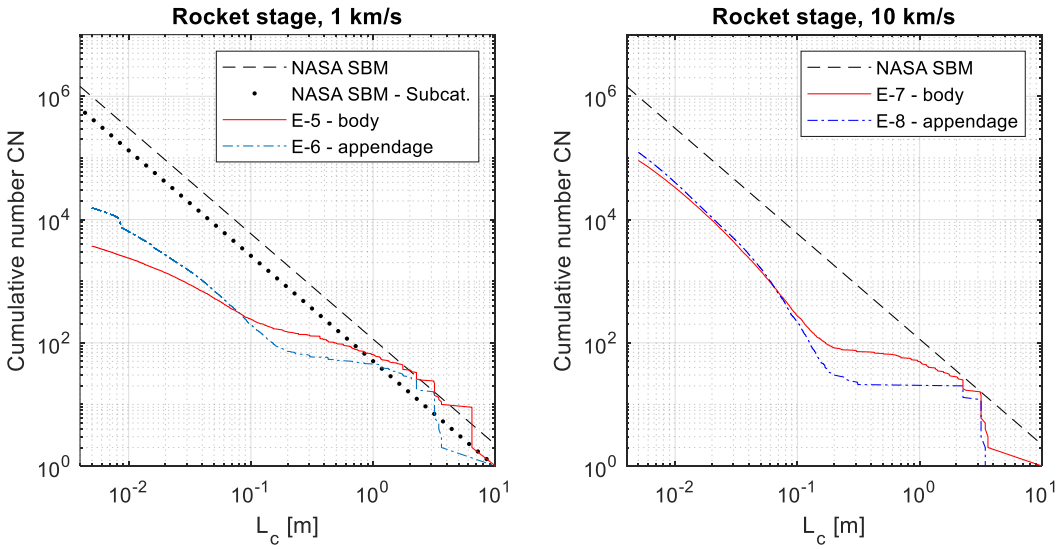


Fig. 7: $L_C$ distribution curves for the second stage impact on ENVISAS at 1 km/s (left, compared to NASA SBM, dashed black line, and NASA SBM subcatastrophic, dotted black line) and at 10 km/s (right, compared to NASA SBM, dashed black line). Impact on ENVISAT centre of mass is reported with the red solid line, impact on the appendage with the blue dashed-dotted line.

scenarios and compare them with the NASA Standard Breakup Model. As stated before, for the low-velocity impacts, the EMR is always under the catastrophic fragmentation threshold of 40 kJ/kg; in this case the comparison with the NASA SBM subcatastrophic model is also reported. It shall be underlined that the characteristic length is the arithmetic mean of the three dimension of a fragment, therefore despite a resolution of 1 cm in fragments size the minimal characteristic length can reach about 5 mm. In fact, nail-shaped or plate-shaped fragments with one or two dimensions larger than the resolution threshold can have a smaller characteristic length.

Distributions from scenarios E-1 and E-2 are reported in Fig. 6, left, representing small satellite collisions at 1 km/s respectively on ENVISAT body and appendage. It can be noted that the two curves are similar, with only a slight higher number of fragments in the class < 3 cm for scenario E-1. In both cases the distribution curves are well below both the NASA

SBM and the NASA SBM subcatastrophic curves for characteristic lengths respectively < 1 m and < 10 cm.

In a similar fashion, Fig. 6, right, reports fragments distributions for scenarios E-3 and E-4, representing the same collision geometry of the previous cases but at 10 km/s. In this case, it can be noted that the number of fragments is generally higher than in scenarios E-1 and E-2 but still below the NASA SBM curve for dimensions < 1 m, despite an EMR of 78.1 kJ/kg, above the currently employed threshold for catastrophic fragmentation of 40 kJ/kg. Furthermore, the impact on ENVISAT appendage (E-4) creates a larger number of small fragments (< 10 cm) with respect to the collision on the spacecraft body (E-3).

Collisions involving the rocket stage are reported in Fig. 7. On the left, the comparison between the impacts on ENVISAT body (E-5) and appendage (E-6), both at 1 km/s, indicates a higher number of smaller fragments (<10 cm) for the second case. In both cases, the number of fragments is larger with respect to scenarios E-1 and E-2, due to the larger mass of the impacting body, but still below the NASA SBM and NASA SBM subcatastrophic curves for characteristic lengths < 1 m.

A similar pattern can be seen for scenarios E-7 (impact on body) and E-8 (impact on appendage), both involving the rocket stage and velocity of 10 km/s, reported in Fig. 7, right. For these scenarios the EMR is the highest (3125 kJ/kg), well above the catastrophic fragmentation threshold. In general, distributions are higher with respect to the other scenarios, again with a slight larger number of small fragments (< 5 cm) for the appendage impact (E-8), and again below the NASA SBM prediction for all fragments distributions.

### *3.2 Area to mass distributions*

In addition to the characteristic length distributions, CSTS elaborates Area-to-mass ratio distributions for the simulated impacts; Fig. 8 shows the comparison of different scenarios.

The plot on Fig. 8, top left, compares the A/m ratio distribution for the two impact points (ENVISAT centre of mass, blue, and appendage, dark khaki) for the small satellite collision at 1 km/s. It can be observed that the distribution peak for the E-1 scenario is more prominent (i.e. it has a larger number of fragments) with a peak at 0.07 $m^2$/kg, while the appendage impact (E-2) shows two peaks, around 0.02 and 0.13 $m^2$/kg. This difference can be clearly correlated to the shielding effect of the appendage: first, the small satellites impacts and fragments the solar panel, creating a large number fragments with a large area to mass (peak at 0.13 $m^2$/kg); in a second time, the residual debris collide with the ENVISAT body with enough energy to break it apart, creating

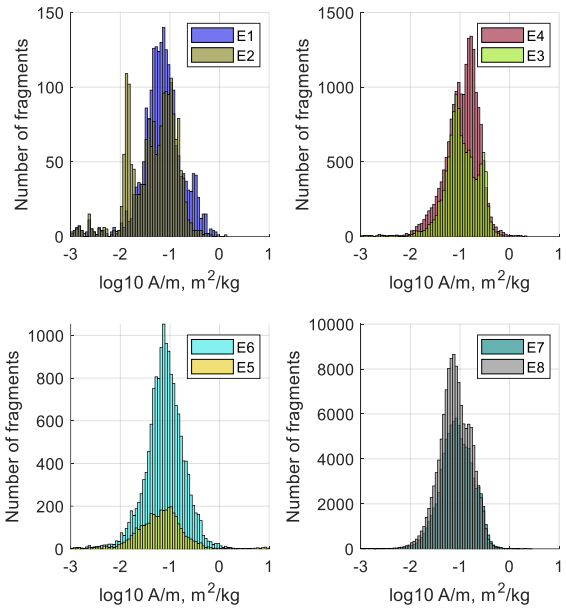


Fig. 8: Comparison of area to mass distributions for different scenarios with same impactor and impact velocity.

bulkier fragments with no fine fragmentation (peak at 0.02 $m^2$/kg). Comparing the characteristic length curves in Fig. 6, left, to the A/m ratio in Fig. 8, top left, it can be observed that similar $L_c$ distributions do not imply comparable A/m ratio ones.

The comparison of a more energetic impact is reported in Fig. 8, top right. In this case the number of fragments of scenario E-3 (light green) is inferior to E-4 (burgundy) and therefore the distribution has a smaller peak. A finer fragmentation of the involved spacecraft with respect to scenarios E-1 and E-2 can be deducted from the two distributions; the more prominent peak for case E-4 is representative of the larger number of generated fragments. While the distribution for scenario E-3 is a scaled-up representation of case E-1, the finer fragmentation of case E-4 produces a bell-shaped curve (with a small secondary peak) different from the one from scenario E-2.

In a similar fashion, distributions for the most energetic impact (EMR of 3125 kJ/kg) can be compared in Fig. 8, bottom right. The two distributions are similar in shape, suggesting a fine fragmentation of the involved body, with a more prominent peak for the impact on ENVISAT appendage (case E-8, about 27% more fragments).

Comparison between scenarios E-5 (yellow) and E-6 (aqua) can be seen in Fig. 8, bottom left. In this case it can be noted that the shape of the distributions is similar, with only a small shift of the peak to lower A/m ratios; on the contrary, in this case the effect of the impact point on fragments number is clear, with

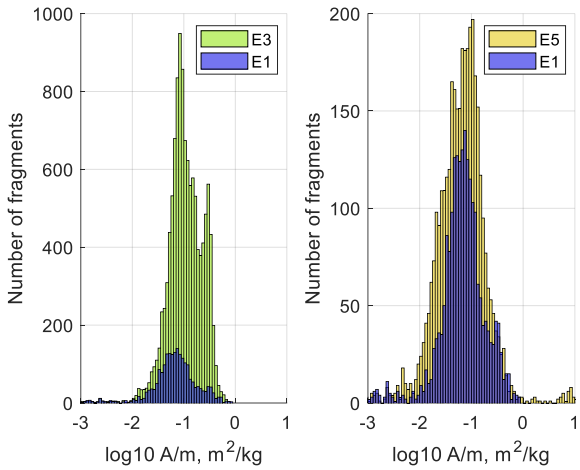


Fig. 9: Comparison between collisions on ENVISAT body for different impact velocities (left) and impactor mass (right).

more fragments generated in scenario E-6 (impact on appendage).

Fig. 9 compares distributions between collisions on ENVISAT body for different impact velocities (left, scenarios E-1 and E-3) and impactor mass (right, cases E-1 and E-5). In the first comparison (Fig. 9, left) it can be noted that while the shape and the position of the peak are comparable, the effect of the velocity can be clearly observed in the different number of generated fragments. Fig. 9, right, suggest that the different impactor can strongly influence the distributions: the collision with the rocket stage (E-5) creates a larger number of fragments; the shape of the area to mass curve is wider and a secondary peak at about 0.03 $m^2/kg$ can be detected with respect to scenario E-1 (small satellite). A more detailed comparison between scenarios E-1 and E-5 is reported in Fig. 10, in function of fragments characteristic length. It can be noted that the peaks of the area to mass distributions both at $L_c$ smaller than 0.01 m (top, red) and between 0.01 and 0.1 m (centre, yellow) are more prominent and at higher values of A/m for scenario E-5 (rocket stage), indicating a finer fragmentation of the colliding objects. This behaviour is still partially recognizable in the class 0.1 to 1 m (bottom, green): for scenario E-1 the number of fragments in this size class is about 130, while for case E-5 they rise to about 170.

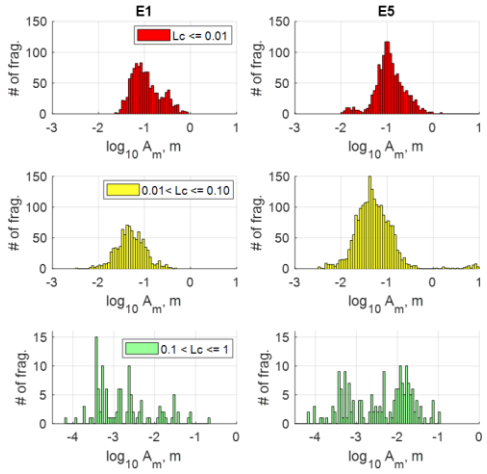


Fig. 10: Comparison of different area to mass distributions for cases E-1 and E-5 at different values of fragments characteristic length.

## 4 Fragmentation cloud propagation

Based on the work in [32][33], an efficient method is developed to describe the evolution in time of the fragmentation cloud resulting from the collision. The algorithm implementing this method is structured according to the following blocks (see Fig. 11):

- The CSTS ENVISAT breakup model, that characterises the fragments generated from the collision, in terms of characteristic length, area-to-mass ratio and velocity.
- A numerical long-term propagator to determine the evolution in time of the orbital elements of the produced fragments, until the continuum formulation in [34] becomes applicable.
- The spatial density function, defined to translate the orbital parameters of each single fragment into a continuous function depending only on the altitude.
- A numerical propagator to describe the evolution in time of the spatial density function, from the band formation instant onward.

### *4.1 Band formation and numerical propagation*

#### 4.1.1 Phases of the evolution of a debris cloud in LEO

The dispersion model of a fragmentation cloud in LEO can be divided into four phases, according to [33]. In the first phase, right after the collision, the produced fragments form an ellipsoid-shaped cloud concentrated at the location where the fragmentation event took

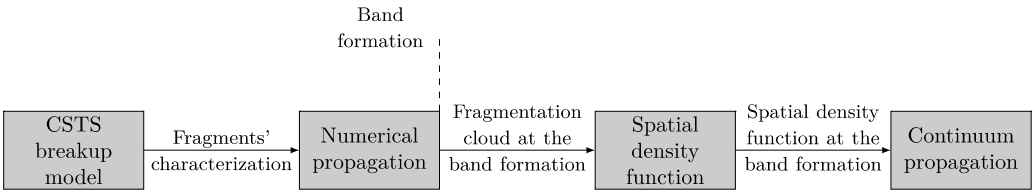


Fig. 11: Schematics of the algorithm for the propagation of the fragmentation cloud.

place. The energy differences among the generated fragments and, hence, their variable orbital periods, cause the initial cloud to be spread out along the parent orbit, forming a toroid (phase two). During phase three, the toroid is gradually dismantled, due the change of the right ascension of the ascending node, Ω, and the variation of the argument of perigee, $\omega$, both caused by the Earth's oblateness. In the final configuration (phase four), the cloud forms a band around the Earth, limited in latitude by the inclination of the parent orbit. Throughout this phase, atmospheric drag can be considered the dominant perturbation [33], since $\omega$, Ω and the true anomaly, $\theta$, are randomised. Consequently, the continuum formulation in [34], which takes into account only the atmospheric drag effect, can be applied only after the band formation, while a numerical propagator is needed to follow the first phases of the cloud evolution.

Considering the approach adopted in [32], the band formation time is estimated as $T_B = 3\,T_b$, where $T_b$ is the expression for the band formation time proposed by Ashenberg [36]. $T_b$ is defined as the maximum between the time of dispersion of the argument of perigee, $T_\omega$, and the time of dispersion of the right ascension of the ascending node, $T_\Omega$.

#### 4.1.2 Numerical propagation

Once the fragments are generated and characterised, their associated position and velocity vectors are computed. Then, the Keplerian elements defining each fragment orbit right after the collision are obtained.

The evolution in time of the fragments' Keplerian elements is computed from the numerical integration of Gauss' planetary equations [37], considering atmospheric drag and Earth's oblateness perturbations. Drag effect is estimated assuming an exponential density model [37]:

$$\rho = \rho_{ref} \exp\left(-\frac{h - h_{ref}}{H}\right) \qquad (1)$$

where $\rho$ is the atmosphere density, $h$ is the altitude and $h_{ref}$ is the reference altitude where the reference density $\rho_{ref}$ and the scale height $H$ are defined. The reference values are taken from [37]. Following the approach in [32], in this work, the reference altitude $h_{ref}$ is selected as the closest tabulated value to the altitude where the fragmentation event takes place and its value is kept constant for the entire simulation; drag effect is considered up to a 1000-km altitude and atmosphere rotation is not taken into account.

The effect of atmospheric drag is computed through the expressions reported in [38], describing the secular variation of the orbital elements. Regarding the Earth's oblateness perturbation, only the long-term effect of $J_2$ is considered. This assumption is made since, over the long-term, the Earth's oblateness only affects $\omega$ and Ω and, consequently, high-precision modelling of this perturbation is not essential.

The numerical integration process is halted if the fragment perigee altitude falls below 50 km, since, under this condition, the fragment is considered to have re-entered through the atmosphere [32].

In Fig. 12, the Gabbard diagrams characterising the initial fragmentation clouds are shown, for all the different scenarios. Note that, in the figure, the fragments with perigee altitudes below 50 km are represented in red. As an additional remark, in Scenarios E-3, E-4, E-7 and E-8, some fragments with eccentricity values higher than one are generated. However, the fact that the proposed formulation cannot deal with these fragments does not represent a limitation. Following their parabolic and hyperbolic orbits, the fragments will escape before the band is formed and, hence, they will have no contribution to the spatial density function. Therefore, they are discarded from the set of produced fragments.

### *4.2 Spatial density function*

Once the band is formed, the information on each single fragment is translated into a total continuous density function.

Here, the spatial density function is built on the probability of finding a fragment at a distance $r$ from the centre of the Earth, given the semimajor axis $a$ and the eccentricity $e$ of its orbit. Taking the expression reported in [39], the spatial density function $n_i(r)$ defining the contribution of fragment $i$ is

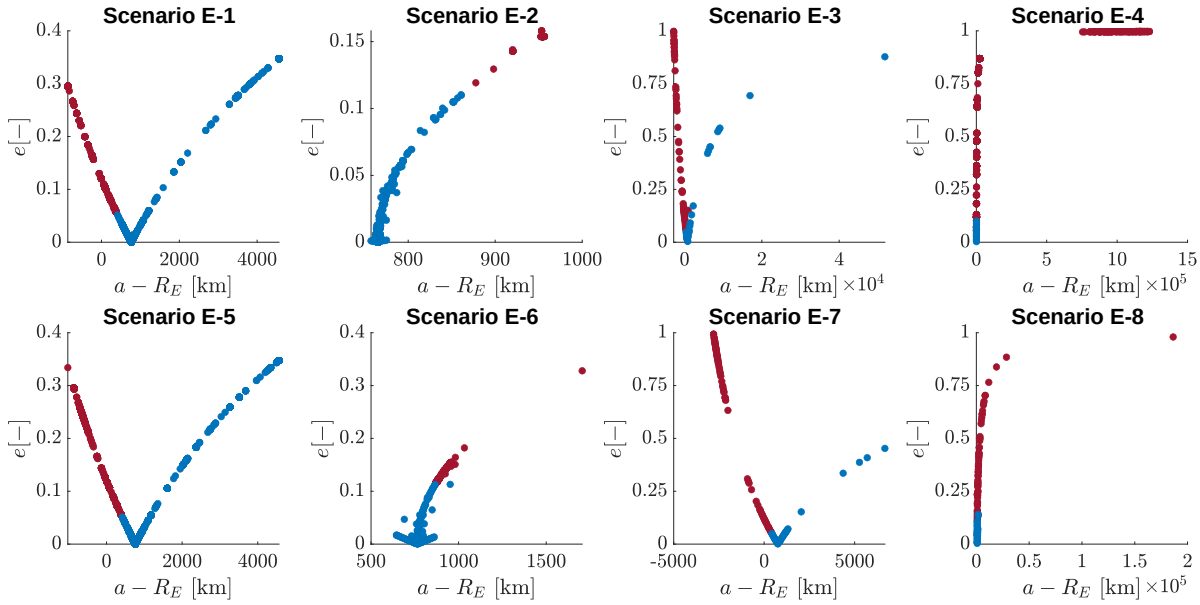


Fig. 12: Distribution of semimajor axis, $a$, and eccentricity, $e$, at the band formation. In the figure, $R_E$ denotes the mean Earth's radius. Fragments with perigee altitudes below 50 km are represented in red.

$$n_i(r) = \frac{1}{4\pi^2 r a_i \sqrt{(r - r_{p_i})(r_{a_i} - r)}} \tag{2}$$

where $r_{p_i}$ and $r_{a_i}$ are, respectively, the periapsis and the apoapsis of the fragment's orbit:

$$r_{p_i} = a_i(1 - e_i) \quad r_{a_i} = a_i(1 + e_i) \tag{3}$$

In order to build the total spatial density function, used as initial condition for the continuum propagation, the contribution of each fragment in the fragmentation cloud must be considered:

$$n(r) = \sum_{i=1}^{N} n_i(r) \tag{4}$$

where $N$ is the total number of objects constituting the fragmentation cloud at the band formation.

### *4.3 Continuum propagation*

Once the spatial density function is built at the band formation instant, the continuity equation is used to compute the density function evolution in time, under the effect of atmospheric drag. Here, the approach developed by McInnes [34] is followed. However, instead of using the analytical expression therein for the density function propagation, the differential equations are numerically integrated, from the band formation instant onward.

Assuming that no discontinuous events occur (sources, like launches; or sinks, as active debris removal), the continuity equation can be written as

$$\frac{\partial n}{\partial t} + \nabla \cdot \mathbf{f} = 0 \tag{5}$$

where $n$ is the density function, $t$ is the time and the term $\nabla \cdot \mathbf{f}$ models the involved continuous phenomena, in this case, the atmospheric drag [34]. In this approach, the radial distance $r$ is the only spatial coordinate, so spherical symmetry is assumed. For that reason and since the atmospheric drag is the only considered perturbation, this formulation is only applicable after the band formation.

The vector field has then only one component:

$$f_r = v_r n(r, t) \tag{6}$$

where $v_r$ is the drift velocity in the radial direction due to drag.

According to the derivations in [32], under the hypothesis of quasi-circular orbits, $v_r$ can be written as

$$v_r = -\varepsilon \sqrt{r} \exp\left(-\frac{r - R_h}{H}\right) \tag{7}$$

with $R_h = R_E + h_{ref}$, and the parameter $\varepsilon$ collecting all the terms that do not depend on $r$:

$$\varepsilon = \sqrt{\mu_E} c_d \frac{A}{M} \rho_{ref} \tag{8}$$

where $\mu_E$ is the Earth's gravitational constant; $c_d$ is the drag coefficient of the fragment, assumed to be

constant and equal to 2.2 [37]; $A$ is the fragment cross-sectional area; and $M$ is the fragment mass.

Through the method of the characteristics, the continuity equation (Eq. 5) can be written as a system of ordinary differential equations describing the time evolution of the density function along the characteristic lines:

$$\frac{dr}{dt} = v_r = -\varepsilon\sqrt{r}\exp\left(-\frac{r-R_h}{H}\right)$$
$$\frac{dn}{dt} = -\left[\frac{2}{r}v_r + v_r{}'\right]n(r,t) \quad (9)$$

with initial conditions

$$r(t_0 = T_B) = r_0$$
$$n(r_0, t_0 = T_B) = n_0(r_0) \quad (10)$$

## 5 Fragmentation effect on the background population

For the purpose of studying the effect of a possible ENVISAT fragmentation, the evolution of the entire debris population is analysed, when at a certain instant ENVISAT collision takes place. The IADC population is used as background debris population.

At the initial time, the spatial density function of the background population is computed, and it is propagated in time, following what was described in Section 4.3Continuum propagation. Simultaneously, the CSTS ENVISAT breakup model is used to characterise the fragments generated from the collision, in terms of characteristic length, area-to-mass ratio and velocity. The orbital elements of the produced fragments are propagated up to the band formation, when the continuum approach becomes applicable for the fragmentation cloud. At this time instant, the spatial density function of the fragmentation is built, and its contribution is added to the pre-existing debris population. Finally, the resulting spatial density function is propagated again, obtaining the evolution in time of the total debris population.

In Fig. 13, the spatial density function at the band formation is presented, for scenario E-5, before and after adding the fragmentation's contribution. In this case, the band formation time is 898 days.

The background population is divided into 7 A/M ratio bins, since the area-to-mass ratio is a key parameter determining not only the spatial/temporal evolution of the fragment due to atmospheric drag, but also the severity of a possible future impact [41]. The bins are defined so that each one contains the same number of objects at the initial time.

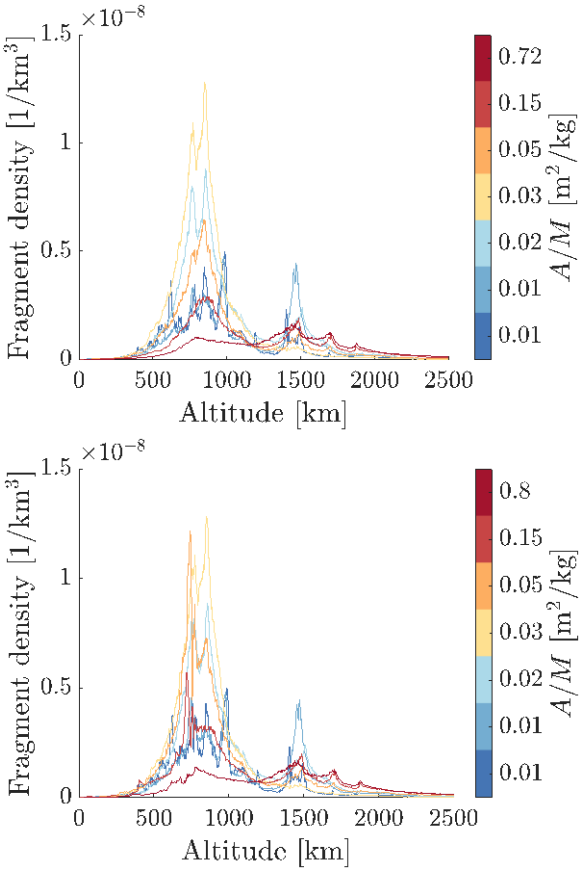


Fig. 13: Spatial density function at the band formation, before (top) and after (bottom) adding the fragmentation's contribution, for Scenario E-5.

As stated before, after the band formation, the assumption of quasi-circular orbits is imposed. To critically assess the accuracy of this hypothesis, the eccentricity distribution at the band formation is presented in Fig. 14, for Scenario E-5. As can be noticed, even if the proposed formulation is not well-suited for highly eccentric orbits, their contribution to the spatial density function is small and, hence, the loss of accuracy can be considered reasonable.

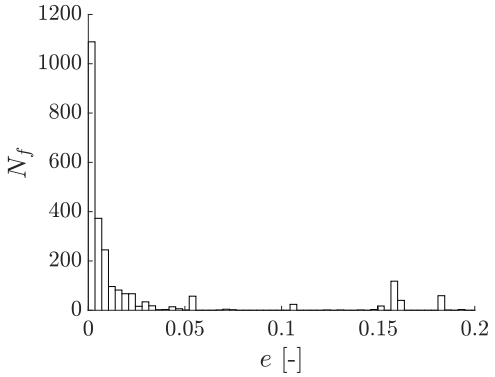


Fig. 14: Eccentricity distribution at the band formation, for Scenario E-5.

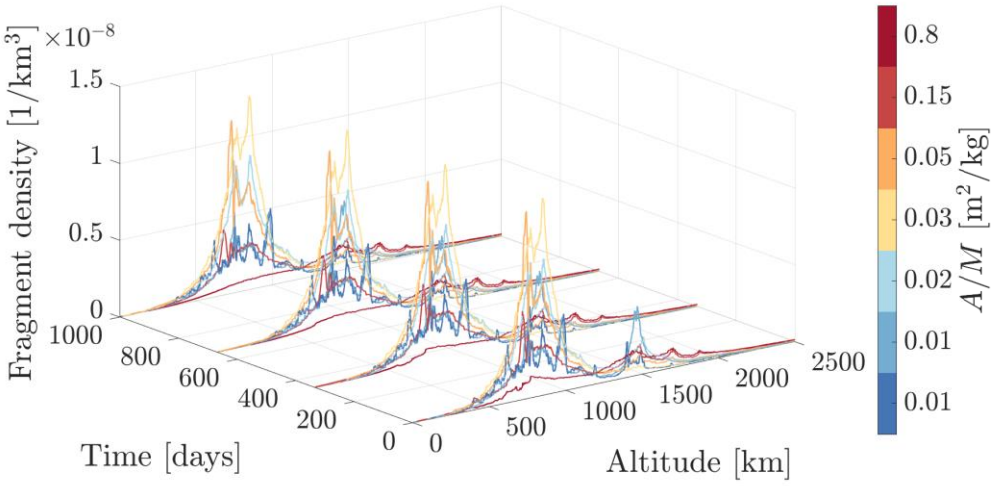


Fig. 15: Evolution of the total density function (time origin set at the band formation instant), for Scenario E-5.

The evolution in time of the total debris population is shown in Fig. 15, from the band formation instant. As can be noticed, ENVISAT fragmentation has a dramatic impact into the total space debris population, with an increase of the spatial density function higher than 400% at the altitude where the collision occurs.

## 6 Conclusions

In this paper eight collision scenarios involving ENVISAT were introduced and the resulting fragments distributions were calculated with the proprietary software CSTS. Results suggested that:

- The NASA SBM may consistently overestimate the number of small and medium sized fragments (< 1 m)
- The subcatastrophic NASA SBM may lead to consistent errors in the number of fragments, by underestimating large fragments and overestimating small ones.

The fragments' orbital propagation is performed for a single relevant scenario (rocket stage impact at 1 km/s on ENVISAT centre of mass). It is shown that a collision with ENVISAT can strongly increase the number of fragments currently in orbit, with an increase of the spatial density function higher than 400% at the altitude where the collision occurs.

**Acknowledgments**

The research work presented in this paper is supported by the Italian Space Agency, in the framework of the ASI-INAF Agreement "Supporto alle attività lADC e validazione pre-operativa per SST (N. 2020-6-HH.0)".

## 7 REFERENCES

[1] Kessler, D. J., & Cour-Palais, B. G. (1978). Collision frequency of artificial satellites: The creation of a debris belt. *Journal of Geophysical Research: Space Physics*, **83**(A6), 2637-2646.

[2] Radtke, J., Kebschull, C., Stoll, E. (2017). Interactions of the space debris environment with mega constellations—using the example of the oneweb constellation. *Acta Astronaut.* **131**, 55–68.

[3] Rossi, A., Alessi, E.M., Valsecchi, G.B., Lewis, H., Radtke, J., Bombardelli, C., Virgili, B.B. (2017). A quantitative evaluation of the environmental impact of the mega constellations. In: *Proc. 7th European Conference on Space Debris*, Darmstadt, Germany.

[4] Virgili, B., Dolado, J., Lewis, H., Radtke, J., Krag, H., Revelin, B., Cazaux, C., Colombo, C., Crowther, R., Metz, M. (2016). Risk to space sustainability from large constellations of satellites. *Acta Astronaut.* **126**, 154–162.

[5] Alvarez, J., & Walls, B. (2016). Constellations, clusters, and communication technology: Expanding small satellite access to space. In *Aerospace Conference*, 2016 IEEE (pp. 1-11). IEEE.

[6] Karacalioglu, A. G., & Stupl, J. (2016). The Impact of New Trends in Satellite Launches on the Orbital Debris Environment. *NASA Technical Report. Houston, TX, United States* (2016)

[7] Foreman, V. L., Siddiqi, A., & De Weck, O. (2017). "Large satellite constellation orbital debris impacts: Case studies of oneweb and spacex proposals." *AIAA SPACE and Astronautics Forum and Exposition*. (p. 5200).

[8] Olivieri, L., & Francesconi, A. (2020). Large constellations assessment and optimization in LEO space debris environment. *Advances in Space Research*, **65**(1), 351-363.

[9] Klinkrad, H. (2017). Large satellite constellations and related challenges for space debris mitigation. *J. Space Saf. Eng*. **4**, 59–60.

[10] Lewis, H.G., Radtke, J., Rossi, A., Beck, J., Oswald, M., Anderson, P., Bastida Virgili, B., Krag, H. (2017). Sensitivity of the space debris environment to large constellations and small satellites. In: *Proc. 7th European Conference on Space Debris*, Darmstadt, Germany.

[11] McKnight, D., Di Pentino, F., & Knowles, S. (2014). Massive Collisions In LEO - A Catalyst To Initiate ADR. In: *Proc. 65th International Astronautical Congress*, Toronto, CA.

[12] Secure World Foundation, 2009 Iridium-Cosmos Collision Fact Sheet, last updated Nov. 10, 2010. https://swfound.org/media/6575/swf_iridium_cosmos_collision_fact_sheet_updated_2012.pdf

[13] Letizia, F., Colombo, C., Lewis, H. G., & Krag, H. (2018). Development of a debris index. In *Stardust Final Conference* (pp. 191-206). Springer, Cham.

[14] Letizia, F., Colombo, C., Lewis, H., & Krag, H. (2017). Extending the ECOB space debris index with fragmentation risk estimation. In: *Proc. 7th European Conference on Space Debris*, Darmstadt, Germany.

[15] McKnight D., Speaks S., Macdonald J., Ebright K. (2018). Assessing Potential for Cross-Contaminating Breakup Events from LEO to MEO/GEO. In: *Proc. 69th International Astronautical Congress*, Bremen, Germany.

[16] Louet J., Bruzzi S. (1999) "ENVISAT mission and system." *IEEE 1999 International Geoscience and Remote Sensing Symposium. IGARSS'99 (Cat. No. 99CH36293)*, **3**, 1680-1682.

[17] ESA Envisat mission page: https://earth.esa.int/web/guest/missions/esa-operational-eo-missions/envisat (Available online Mar. 10, 2021)

[18] Lin, H. Y., & Zhao, C. Y. (2018). An estimation of Envisat's rotational state accounting for the precession of its rotational axis caused by gravity-gradient torque. *Advances in Space Research*, **61**(1), 182-188.

[19] Sommer, S., et al. (2018). Temporal analysis of ENVISAT's rotational motion. In *Proc. 7th European Conference on Space Debris*, Darmstadt, Germany.

[20] Flohrer, T., et al. (2015). Operational collision avoidance at ESOC. *Deutscher Luft-und Raumfahrtkongress, Rostok, Germany* 0270.

[21] Estable, S. (2016). Envisat removal by robotic capture means-results of the airbus ds led e. Deorbit Phase B1 ESA study. *ESA Clean Space Industrial Days, ESTEC, Netherlands*.

[22] Estable, S., et al. (2017) Definition of an Automated Vehicle with Autonomous Fail-Safe Reaction Behavior to Capture and Deorbit Envisat. In *Proc. 7th European Conference on Space Debris*, Darmstadt, Germany.

[23] Hausmann, G., et al. (2015). "E. Deorbit mission: OHB debris removal concepts." *Proceeding of the 13th Symposium on Advanced Space Technologies in Robotics and Automation (ASTRA'2015),* Noordwijk, The Netherlands.

[24] Olivieri, L., Giacomuzzo, C., Duran-Jimenez, C., Francesconi, A., & Colombo, C. (2021). Fragments Distribution Prediction for ENVISAT Catastrophic Fragmentation. In *8th European Conference on Space Debris, ESA/ESOC* (pp. 1-12). ESA.

[25] Francesconi, A., et al. (2019). CST: A new semi-empirical tool for simulating spacecraft collisions in orbit. *Acta Astronautica*, **160**, 195-205.

[26] Francesconi A., et al. (2019) Examination of satellite collision scenarios spanning low to hypervelocity encounters using semi-empirical models, In: *Proc. 70th International Astronautical Congress*, Washington, US.

[27] Sarego G. et al. (2019). Numerical evaluation of the influence of pre-arranged fault lines in the fragmentation of satellites subjected to hypervelocity collisions. *In: Proc. 70th International Astronautical Congress*, Washington, US.

[28] Colombo C., Letizia F., Lewis H. (2016). Spatial density approach for modelling of the space debris population, *26th AAS/AIAA Space Flight Mechanics Meeting*, Fe. 2016, AAS 16-465

[29] https://global.jaxa.jp/projects/sat/sds1/index.html (Available online Mar. 10, 2021)

[30] http://www.braeunig.us/space/specs/lgmarch.htm (Available online Mar. 10, 2021)

[31] Le May, S., et al. (2018). Space debris collision probability analysis for proposed global broadband constellations." *Acta Astronautica*, **151**, 445-455.

[32] Letizia, F., Colombo, C. & Lewis, H.G. (2015). Analytical Model for the Propagation of Small-Debris-Object Clouds After Fragmentations.

*Journal of Guidance, Control, and Dynamics*, **38**(8), 1478-1491.

[33] Duran, C., Giudici, L. & Colombo, C. (2021). Modelling the Whole Space Debris Environment Through a Spatial Density Function. *2021 AAS/AIAA Astrodynamics Specialist Conference Big Sky Virtual.*

[34] McInnes, C. R. (2000). Simple Analytic Model of the Long Term Evolution of Nanosatellite Constellations. *Journal of Guidance, Control, and Dynamics*, **23**(2), 332–338.

[35] Jehn, R. (1991). Dispersion of Debris Clouds from In-Orbit Fragmentation Events. *ESA Journal*, **15**(1), 63-77.

[36] Ashenberg, J. (1994). Formulas for the Phase Characteristics in the Problem of Low-Earth-Orbital Debris. *Journal of Spacecraft and Rockets*, **31**(6), 1044-1049.

[37] Vallado, D. A. (2013). *Fundamentals of Astrodynamics and Applications, 4th ed.*, Springer, New York, NY, pp. 628–637.

[38] King-Hele, D. (1987). *Satellite Orbits in an Atmosphere: Theory and Application*, Blackie, Glasgow, pp. 44–62.

[39] Kessler, D.J. (1981). Derivation of the Collision Probability between Orbiting Objects: The Lifetimes of Jupiter's Outer Moons. *Icarus*, **48**(1), 39–48.

[40] Letizia, F. (2015). *Space Debris Cloud Evolution in Low Earth Orbit*. PhD thesis. University of Southampton.

[41] McKnight, D. S. (1991). Determination of Breakup Initial Conditions. *Journal of Spacecraft and Rockets*, **28**(4), 470–477.